Elliptic flow of anti-protons, kaons and pions in Pb-Pb collisions at $\sqrt{S_{NN}} = 2.76$ TeV

Author:
Manon Verra
Student number: 3938344
Study: Physics and Astronomy

Supervised by:
Prof. dr. R.J.M. Snellings
Dr. A.F. Dobrin

Bachelor thesis
Institute for Subatomic Physics
Faculty of Science
Utrecht University

June 2015

Universiteit Utrecht

Abstract

According to the Standard Model of particle physics all matter is made up of fundamental, point-like particles called quarks and leptons. The quarks interact via the strong force, which is mediated by a gauge boson called the gluon. Quantum Chromodynamics (QCD) describes the interactions between quarks and gluons. QCD predicts a phase transition at high temperatures ($\sim 2 \times 10^{12}\,\mathrm{K}$) and high densities ($\sim 1\,\mathrm{GeV/fm^3}$) to a very hot and dense state of matter consisting of new degrees of freedom, called the Quark Gluon Plasma (QGP). It is believed that a QGP existed shortly after the Big Bang and might still exist in heavy neutron stars.

To study the QGP in the laboratory heavy ions are collided using particle accelerators. ALICE is one of the seven LHC experiments at CERN. Its aim is to study the phase transition to the QGP. The data used for this research is the full sample from run 1 of the LHC Pb-Pb runs in 2010, at a center of mass energy of 2.76 TeV per nucleon-pair.

The QGP cannot be observed directly, but as it expands and cools down hadrons are formed that can be detected. The anisotropy of the azimuthal momentum distribution of the formed hadrons is described by a Fourier expansion of which the second coefficient is called the elliptic flow. In this thesis the elliptic flow of anti-protons, kaons and pions is studied using the scalar product method. The elliptic flow is compared qualitatively with a viscous hydrodynamic model to investigate mass ordering of the particle species. In the first chapter some background information is provided.

Contents

Chapter 1

Theory

All matter consists of elementary particles, which are the building blocks of nature. These elementary particles are described by the Standard Model of particle physics. According to the Standard Model all matter is made up of fundamental particles called leptons and quarks. Leptons are point-like particles, amongst which are the electrons and the neutrino's. *Quarks* are also point-like particles and they are the fundamental constituents of hadrons, like protons and neutrons. Next to leptons and quarks, the Standard Model also includes four kinds of gauge bosons that mediate three of the fundamental forces of nature: the strong force, the weak force and the electromagnetic force. The quarks interact via the strong force, which is mediated by a particle called the *gluon*.

The theory that describes the interactions between the quarks and gluons is *Quantum Chromodynamics* (QCD). The main interesting features of QCD are confinement and asymptotic freedom. When quarks are separated and their relative distance increases, they exchange more gluons and the interaction strength between the quarks increases. Quarks also exchange more gluons at lower temperatures. Due to this behaviour quarks cannot be separated at low densities and low temperatures and free quarks cannot be observed. This is called *confinement*. However, the quarks can be treated as free particles at high densities and high temperatures. This is called *asymptotic freedom*. QCD predicts a phase transition at high temperatures ($\sim 2 \times 10^{12}\,\mathrm{K}$) and high densities ($\sim 1\,\mathrm{GeV/fm^3}$) to a very hot and dense state of matter consisting of new degrees of freedom, called the *Quark Gluon Plasma* (QGP) [1].

Those conditions of high temperature and high density are the conditions that were present at the beginning of the universe, according to the Big Bang theory. In this early stage of the universe, densities and temperatures were so high that hadrons could not be formed and it is believed that a QGP existed at this stage of the universe. As the universe expanded and cooled down, the interaction strength between the quarks increased. Quarks and gluons became confined into hadrons and free quarks and gluons no longer existed. Similar conditions of high temperature and high density are created in the collisions of highly energetic nuclei. By studying the QGP that is created in the laboratory, the same matter is thus being studied that is believed to have existed at the beginning of the universe.

Presently there are not many places left where a QGP might exist and quarks and gluons could still be free particles. One of the options is in very heavy neutron stars. It is believed that inside these stars the densities and temperatures could be high enough for a QGP to exist [2].

1.1 Heavy ion collisions

To create a QGP in the laboratory a large amount of energy and a high density are needed for the quarks to exhibit a phase transition to a deconfined state. The best way to reach these conditions is by using heavy ion collisions in particle accelerators. There are several particle accelerators around the world used for heavy ion collisions. One of them is the Relativistic Heavy Ion Collider (RHIC) at Brookhaven National Laboratory in the United States, which uses primarily gold ions at a center-of-mass energy of 200 GeV per nucleon-pair [3]. In Europe, the Large Hadron Collider (LHC) at the European Organization for Nuclear Research (CERN) is used to study heavy ion collisions. At the LHC lead ions reach collision energies of 2.76 TeV per nucleon-pair [4]. The QGP created in these collisions cannot be observed directly, since it doesn't exist long enough to be measured. But the QGP expands rapidly, and

as it cools down hadrons are created that can be detected.

When the nuclei collide only the nucleons in the overlap region interact and form a QGP. The interacting nucleons in the overlap region that form the QGP are called *participants*. The nucleons outside of the overlap region are called *spectators*. These spectators do not interact with other nucleons and they are not affected by the collision. They thus continue to move with the same momentum they had before the collision. Figure 1.1 shows a collision with spectators and participants.

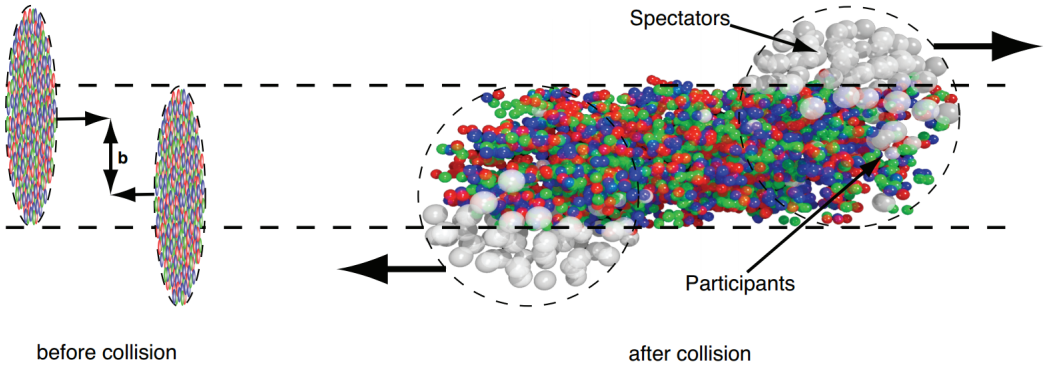

Figure 1.1: *Left: The two nuclei approaching each other before the collision with impact parameter* ***b****. Right: The spectators are not affected by the collision and continue to travel with the same momentum. In the overlap region where the participants interact, hadrons are produced.*

Due to their relativistic speeds, the ions are Lorentz contracted and they approach each other as flat disks. If the particles collide, the overlap region of the nuclei is theoretically described by the impact parameter. The impact parameter **b** is defined as the transverse distance between the centre of the two colliding nuclei, as can be seen in Figure 1.1. Since it is not possible to determine the impact parameter experimentally, the overlap region is described by the *centrality*. There are different conventions for the centrality. In this thesis a centrality of 0% corresponds with a collision that was most central, which is when the nuclei collide head-on and the impact parameter approximates zero. A higher centrality corresponds with a collision that was more peripheral. The maximum possible centrality is 100%, which is when the impact parameter approximates twice the radius of the nucleus.

In order to determine the centrality of a collision the initial geometry of the collision has to be known. The initial geometry cannot be observed, and therefore one has to rely on models in order to obtain it. In this thesis the centrality was determined by fitting the multiplicity distribution with a Glauber model. The *multiplicity* is the number of particles that was created in a collision. The Glauber model treats a collision as a sum of proton-proton collisions. Since for proton-proton collisions experimental data is available, this can be used to determine the initial state conditions that correspond with the measured final state observables [5]. Other models that can be used to determine the initial state of the collision also exist, like the IP Glasma model [6] and the Color Glass Condensate model [7].

Figure 1.2 shows a schematic representation of the time evolution of heavy ion collisions. When the nuclei collide, the participant nucleons interact. Once the system has thermalized, the QGP will start to expand during the *QGP phase*. This collective expansion is called *flow* and is a result of multiple interactions between the constituents [8]. Stronger interactions thus lead to a larger flow. Due to this collective expansion, the QGP cools down and eventually hadrons will be formed. This stage is called the *hadronization*. The hadrons are still interacting with each other between the QGP phase and the kinetic freeze-out. After the kinetic freeze-out the particles are no longer interacting with each other. This is the stage in which the hadrons are detected.

1.2 Anisotropic flow

Since the QGP cannot be observed directly, phenomena that are sensitive to early collision dynamics are studied and give information about the nature of the QGP. When the impact parameter is small and the collision is almost head on, the overlap region is approximately spherical. This approximately

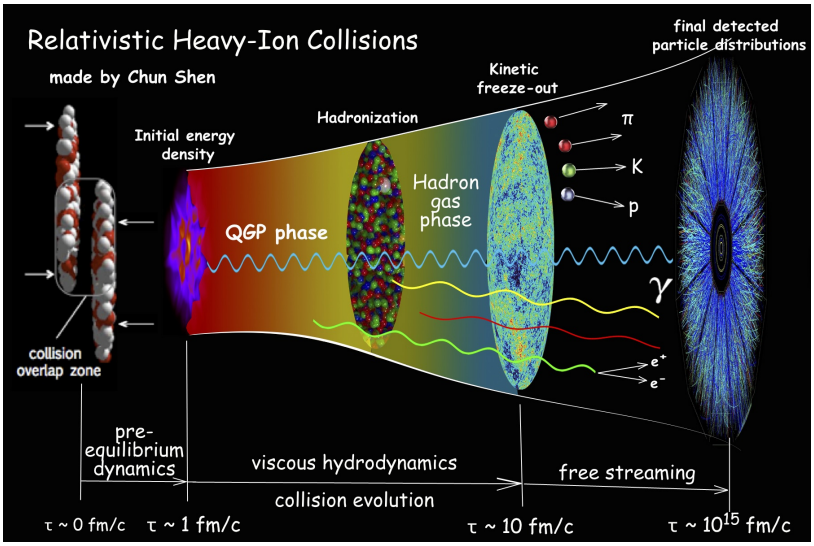

Figure 1.2: *The time evolution of heavy ion collisions. Figure taken from* [9].

azimuthally symmetric spatial distribution results in an approximately azimuthally symmetric expansion of the QGP called *radial flow*. In the case that the collision is more peripheral, the overlap region has an almond shape. This can be seen in Figures 1.3 and 1.4. This azimuthally asymmetric spatial distribution results in an azimuthally asymmetric expansion which is called *anisotropic flow* [10].

Flow is caused by initial pressure gradients in the medium. Due to these pressure gradients the initial spatial anisotropy is converted into momentum anisotropies of the produced particles. Figure 1.3 shows the initial spatial geometry of the overlap region in a non-central collision. The pressure is directed vertically, towards the center of the overlap region and thus causes more particles to propagate into the reaction plane then with an angle with respect to it. The *reaction plane* is the plane spanned by the impact parameter and the beam axis, as can be seen in Figure 1.4.

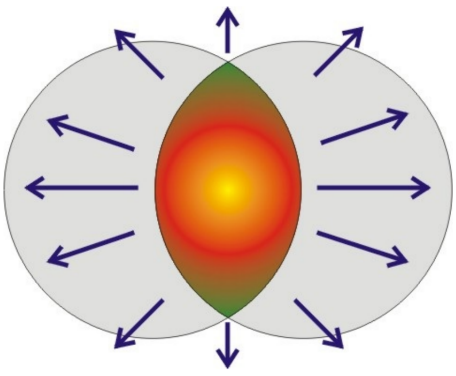

Figure 1.3: *The overlap region of a non-central heavy ion collision. The arrows indicate the direction and the magnitude of the flow. The pressure gradient that causes the flow is directed vertically towards the center of the overlap region. Figure taken from* [11].

The anisotropy of the azimuthal momentum distribution is quantitatively characterized by a Fourier expansion of the momentum distribution, which is given by [12]

$$E\frac{\mathrm{d}^3N}{\mathrm{d}^3p} = \frac{1}{2\pi}\frac{\mathrm{d}^2N}{p_T\mathrm{d}p_T\mathrm{d}y}\left(1+\sum_{n=1}^{\infty}2v_n(p_T,y)\cos[n(\phi-\Psi_R)]\right), \tag{1.1}$$

where E is the energy of the particle, N is the number of particles, p is the momentum, p_T is the transverse momentum, y is the rapidity, v_n is the n^{th} order Fourier coefficient, ϕ is the angle of the track

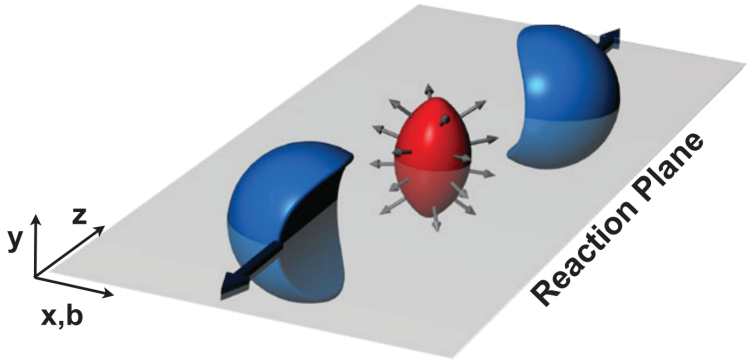

Figure 1.4: *In a non-central collision, the two colliding nuclei (blue) produce an almond-shaped overlap region (red). Figure taken from [8].*

and Ψ_R is the reaction plane angle. The Fourier coefficients $v_n(p_T, y)$ are given by

$$v_n(p_T, y) = \langle \cos[n(\phi - \Psi_R)] \rangle, \tag{1.2}$$

of which v_1 is the *directed flow*, v_2 is the *elliptic flow* and v_3 is the *triangular flow*. In this thesis only the elliptic flow is studied. The elliptic flow coefficient is a measure of how elliptic the overlap region between the nuclei was in two dimensions, or almond-shaped in three dimensions. A larger ellipticity leads to a larger elliptic flow.

The *rapidity* is defined as

$$y \equiv \frac{1}{2} \ln \left(\frac{E + p_z}{E - p_z} \right), \tag{1.3}$$

where p_z is the z-component of the momentum. Related to the rapidity is the *pseudo-rapidity*, which is a spatial coordinate often used in particle physics, instead of the polar angle θ. The pseudo-rapidity is defined as

$$\eta \equiv -\ln \left[\tan \left(\frac{\theta}{2} \right) \right], \tag{1.4}$$

such that when θ equals zero, η approaches infinity and when θ equals $\frac{\pi}{2}$, η equals zero. Due to the symmetry around $\theta = \pi/2$, the pseudo-rapidity can take on both positive and negative values. The pseudo-rapidity can also be written as

$$\eta = \frac{1}{2} \ln \left(\frac{|\mathbf{p}| + p_z}{|\mathbf{p}| - p_z} \right), \tag{1.5}$$

where $|\mathbf{p}|$ is the particles three-momentum. For highly relativistic particles $E \approx |\mathbf{p}|$ and $y \approx \eta$.

1.2.1 The scalar product method

Unfortunately, although the angles ϕ with respect to the laboratory frame are known, the reaction plane angles Ψ_R are not. Different methods have been developed to estimate the v_n coefficients. Some of these methods rely on the explicit reconstruction of the reaction plane. The method used in this thesis is the *scalar product method*. This method does not reconstruct the reaction plane. Instead it uses two particle correlations to estimate the v_n. However, not only the anisotropic flow contributes to the two particle correlations. *Non-flow effects* such as jets, resonance decays and momentum conservation also contribute, and the anisotropic flow will be overestimated due to these effects [13]. These effects are mostly present for few particle correlations and will thus decrease for increasing multiplicities.

Before starting with a more quantitative description of the scalar product method the concepts of the *unit flow vector* and the *Q-vector* will be introduced.

The unit flow vector u_n of the i'th particle is given by

$$u_{n,i} = \mathrm{e}^{in\phi_i}. \tag{1.6}$$

The Q-vector of an event is defined as

$$Q_n \equiv \sum_i^M \mathrm{e}^{in\phi_i}, \tag{1.7}$$

where the sum runs over all particles i in an event with multiplicity M.

The Q-vector can be written in terms of non-complex components $Q_{n,x}$ and $Q_{n,y}$ as $Q_n = Q_{n,x}+iQ_{n,y}$, with $Q_{n,x}$ and $Q_{n,y}$ given by

$$Q_{n,x} = \sum_i \cos(n\phi_i) \tag{1.8}$$

$$Q_{n,y} = \sum_i \sin(n\phi_i). \tag{1.9}$$

In the scalar product method, all particles in an event are divided into either *reference particles* (RP's) or *particles of interest* (POI's). The method requires an abundant source of particles as RP's. In this thesis the RP's were chosen to comprise all tracks and the POI is one specific particle, that is thus correlated with all the other tracks. The method requires that the RP's are divided into two uncorrelated subsets a and b. In this thesis the tracks were divided over these subsets randomly.

In order to calculate v_n, the unit flow vector $u_{n,i}$ of the i'th POI is correlated with the complex-conjugate Q-vector of the RP's. The v_n coefficients can then be written as

$$v_n(p_T, y) = \frac{\left\langle \left\langle u_{n,i}(p_T, y) \frac{Q_n^*}{M} \right\rangle \right\rangle}{\sqrt{\left\langle \frac{Q_n^a}{M_a} \frac{Q_n^{b*}}{M_b} \right\rangle}}, \tag{1.10}$$

where Q_n^a, Q_n^b are the Q-vectors of RP's in subsets a, b. The i'th track is removed from the Q_n^*-vector in order to remove auto-correlations. The Q-vectors are divided by the multiplicity M in order to remove the multiplicity fluctuations. The upper part of v_n is averaged twice, over all tracks and all events, whereas the lower part is averaged only over all events.

The elliptic flow v_2 can provide information about the initial state of a heavy-ion collision. By comparing the obtained results with initial state models the transport properties of the QGP (η/s) and the equation of state can be determined. By calculating v_2 after particle identification information about the particle production can be deduced and the results can be compared with the hydrodynamic model, quark coalescence and jet quenching, which will be treated in more detail in the following section.

1.3 Modelling the QGP

Although the quarks and gluons are described by QCD, this theory cannot be used to calculate particle dynamics in heavy-ion collisions [5]. Instead one has to rely on models.

In the hydrodynamic model the QGP is treated as a fluid and is described by an equation of state of the form $P = P(\epsilon, n)$, where P is the pressure, ϵ is the energy density and n is the baryon number density. An ideal fluid description for the QGP was tried, but this lead to a v_2 that is not in agreement with the data. Instead, the QGP is described as a fluid with a very small viscosity. This viscosity is so small that the QGP would be the most nearly perfect fluid known. To describe the viscosity of the QGP the dimensionless *kinematic viscosity* ν is used, which is defined as the shear viscosity over entropy ratio, $\nu = \eta/s$ [4]. The hydrodynamic model predicts mass ordering of the particle species, as can be seen in Figure 1.5. Mass ordering is caused by the fact that the radial flow shifts the p_T distributions to larger values of p_T. This effect increases with particle mass, and thus for fixed p_T particles with increasing mass have decreasing values of v_2 [14]. The viscous hydrodynamic model has shown to give reliable results for low transverse momentum, $p_T \lesssim 3$ GeV/c. The assumptions on which the hydrodynamic model relies cause it to be less accurate for higher p_T.

For intermediate p_T, approximately between 3 GeV/c and 8 GeV/c, a mechanism called *quark coalescence* is needed to give a more accurate description of the QGP. Low momentum quarks in the QGP will combine to form baryons and mesons. Baryons are particles that consist of three quarks, mesons are particles that consist of a quark and an anti-quark. At a fixed momentum, it is easier to form a baryon

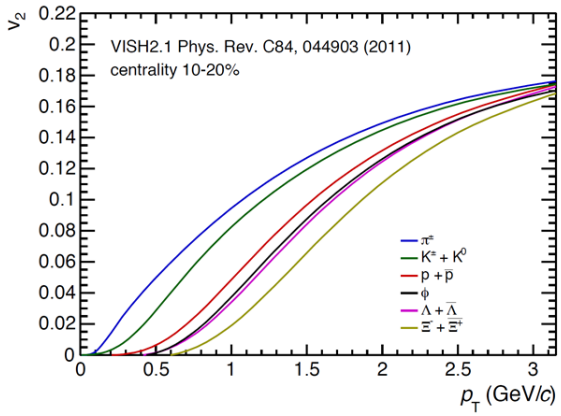

Figure 1.5: The elliptic flow coefficient v_2 as predicted by the hydrodynamic model for different particle species. The hydrodynamic model predicts mass ordering between different particle species. Figure taken from [15].

from three low momentum quarks than a meson from two higher momentum quarks, since there are more quarks with low momentum. This has the effect to increase the baryon/meson ratio. The extra baryons and mesons from the quark coalescence increase v_2, and thus the baryon v_2 is relatively increased more than the meson v_2. Since in the quark coalescence mechanism the baryons and mesons are assembled from free quarks, quark coalescence indicates that the system is in a deconfined state [14].

For higher p_T another mechanism is used to describe the QGP, which is called *jet quenching*. A quark can radiate a gluon, which in turn can produce a quark-antiquark pair ($q\bar{q}$). When the distance between the quarks in this $q\bar{q}$ pair increases, more $q\bar{q}$ pairs will be formed, due to the confinement of the quarks. These extra $q\bar{q}$ pairs can in turn also radiate gluons and produce extra $q\bar{q}$ pairs. A lot of particles will thus be produced in roughly the same direction, causing a so called *jet*. This radiative energy loss depends strongly on the traversed path length of the propagating quark or gluon. In a non-central collision, the overlap region is almond shaped and the propagating particles thus traverse different path lengths, depending on their azimuthal angle. Therefore the production of particles due to jet quenching is azimuthally anisotropic and has the effect to give a v_2 [16]. This mechanism is dominant for $p_T \gtrsim 8$ GeV/c.

Chapter 2

Experimental Setup

2.1 The CERN accelerator complex

To make a QGP in the laboratory highly energetic nuclei are collided using particle accelerators. The largest particle physics laboratory in the world is operated by CERN and currently consists of six accelerators and a decelerator. Figure 2.1 shows the accelerator complex. Before the heavy ions collide, the ions travel a long way in CERN's accelerator complex [17]. The ions, obtained from a source of vaporized lead, begin their journey in the Linac 3 linear accelerator. After being accelerated by the Linac 3 to a collision energy of 4.2 MeV/u, the ions are accelerated successively by the Low Energy Ion Ring (LEIR), the Proton Synchroton (PS) and the Super Proton Synchroton (SPS) to collision energies of up to 176.4 GeV/u. Then they are passed on to the LHC, which accelerates them to their final energy of currently 1.38 TeV/u.

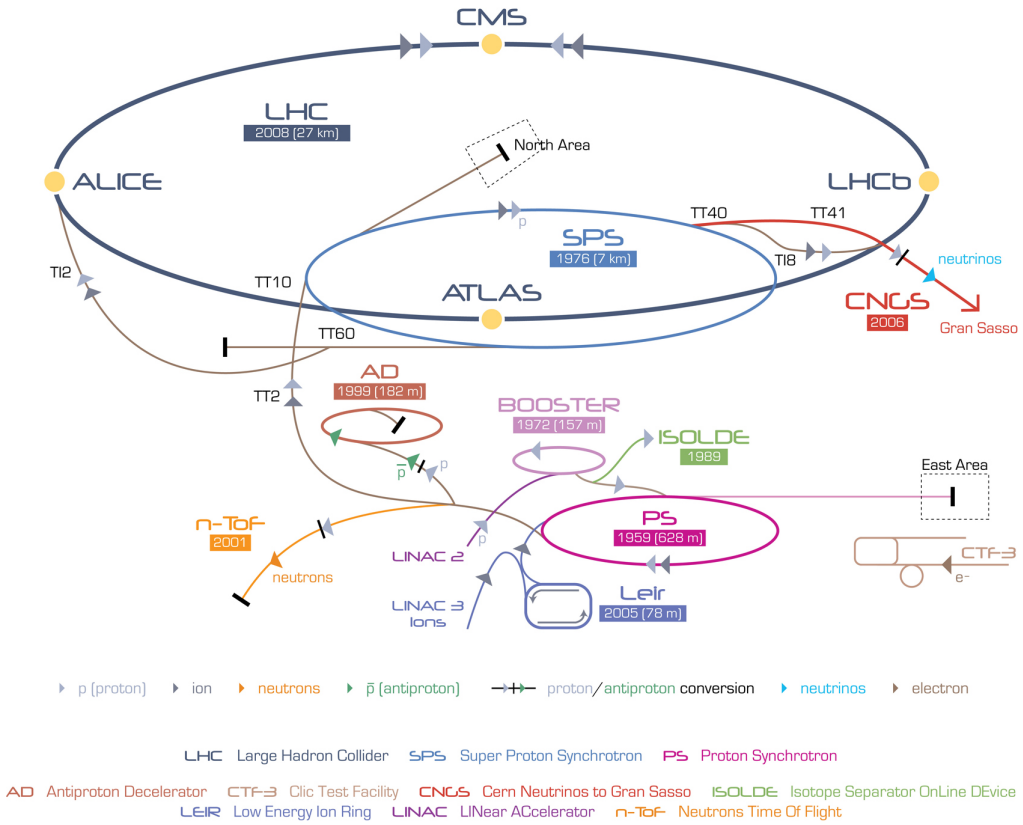

Figure 2.1: *The CERN accelerator complex. Lead ions are successively accelerated by the Linac 3, LEIR, SP and SPS before they are injected into the LHC. Figure taken from* [18].

The LHC started operating in 2010 and with its 27 kilometres circumference it has since been the world's largest and most powerful particle accelerator. The LHC is used to test the Standard Model of particle physics and research dark matter, antimatter, the Higgs boson, supersymmetry and the Quark Gluon Plasma. The LHC has two beam pipes, in which the beams are travelling in opposite direction. The beams cross each other in four straight sections of the LHC ring. These collision points are the locations of the four biggest detectors: ALICE, ATLAS, CMS and LHCb. In this thesis only the ALICE detector is used, which will now be covered in more detail.

2.2 A Large Ion Collider Experiment

A Large Ion Collider Experiment (ALICE) is a general-purpose, heavy-ion detector designed to study matter at extremely high energy densities, where it is expected to exhibit a phase transition to a Quark Gluon Plasma [4]. The ALICE detector was built by the ALICE Collaboration, which currently consists of over 1500 scientists, coming from 151 institutes in 37 countries. The tracking system of the ALICE detector covers a large momentum range, from tens of MeV/c to over 100 GeV/c. These tracks can be identified using practically all known particle identification (PID) techniques: energy loss $\mathrm{d}E/\mathrm{d}x$, time-of-flight, transition and Cherenkov radition, electromagnetic calorimetry, muon filters and topological decay reconstruction. In this thesis only energy loss and time-of-flight will be used for PID. For the ALICE detector a general coordinate system exists, that will also be used in this thesis and can be found in Appendix A.

The ALICE detector consists of a central barrel that is used to measure hadrons, electrons and photons, and a forward spectrometer that is used for the identification of muons. The central barrel is located in the L3 magnet, which provides a magnetic field with a strength of up to 0.5 T. Both the central barrel and the forward spectrometer consist of several subdetectors, which all serve a different purpose in the experiment. Figure 2.2 shows the 10,000-tonne, 26 m long, 16 m wide and 16 m high ALICE detector with all of its subdetectors. Of these subdetectors the Inner Tracking System, Time Projection Chamber and Time Of Flight from the central barrel and the forward detector VZERO are of most importance for this thesis and will be treated in more detail in the remaining of this chapter.

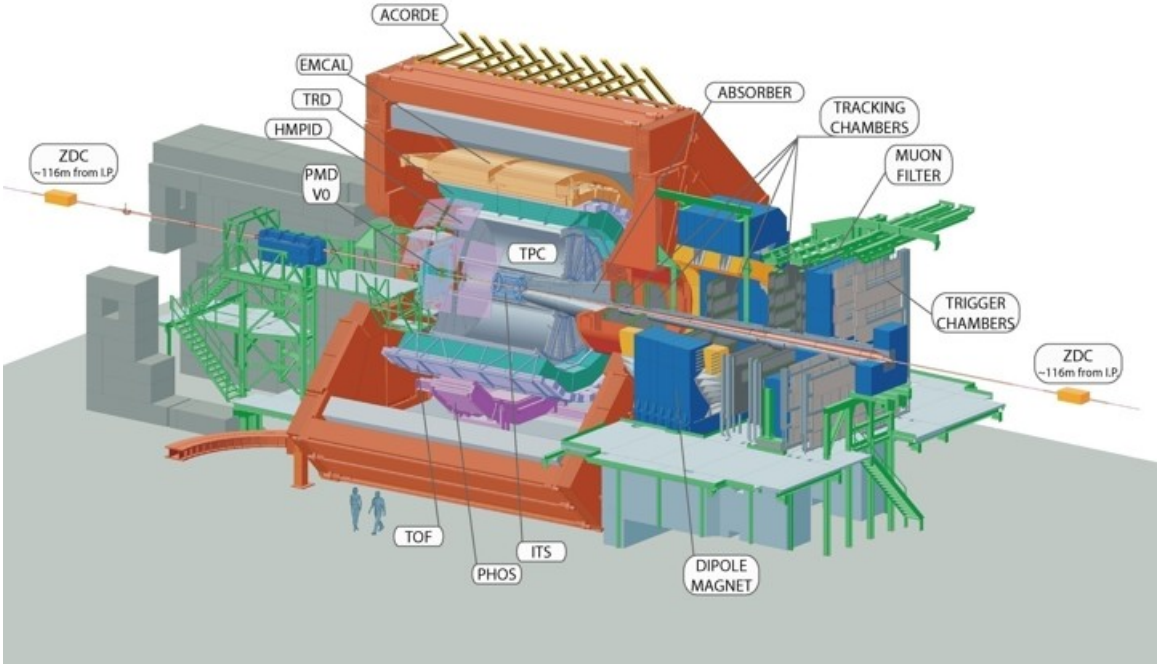

Figure 2.2: *The ALICE detector with the central barrel in red and the forward spectrometer to the right of the central barrel. Figure taken from* [19].

2.2.1 Inner Tracking System (ITS)

The Inner Tracking System is a cylindrical detector that surrounds the beam pipe. The detector consists of six layers with radii between 3.9 cm and 43 cm. The ITS provides data for the reconstruction of the primary vertex with a resolution better than 100 μm, the reconstruction and identification of tracks with momentum below 200 MeV/c and the determination of the Distance of Closest Approach. The *primary vertex* or *reconstructed vertex* is the collision point and is reconstructed from the determined particle tracks. All particles coming from this point are called *primaries*. *Secondaries* are particles that do not come from the primary vertex, but from decays of primaries and material interactions. The *Distance of Closest Approach (DCA)* is the minimum distance between the track and the primary vertex. In this thesis the DCA is used to reject secondaries.

The ITS covers the pseudo-rapidity range $|\eta| < 0.9$. Only the two innermost layers cover an extended pseudo-rapidity range, which is $|\eta| < 2$ and $|\eta| < 1.4$ for the first and second layer, respectively. The ITS covers the full azimuthal angle.

From inside out, a particle crossing the ITS first reaches two layers of Silicon Pixel Detector (SPD). The SPD layers play a fundamental role in the determination of the position of the primary vertex and are used for triggering. In this thesis the SPD layers are also used for centrality determination. Next, the particle will cross two layers of Silicon Drift Detector (SDD). The last two layers that the particle will cross are the Silicon Strip Detectors (SSD), which are used to match tracks from the ITS to tracks from the TPC.

2.2.2 Time Projection Chamber (TPC)

The Time Projection Chamber is a cylindrical detector with an inner radius of 0.85 m and an outer radius of 2.5 m that surrounds the ITS coaxially. The pseudo-rapidity range of the TPC is $|\eta| < 0.9$ and it covers the full azimuthal angle. The TPC is filled with 90 m^3 of a $NeCO_2N_2$ gas mixture.

Particles that cross the TPC will ionize the gas along their track. As a result of this the particles lose an amount of energy per unit track length. This energy loss is particle specific and can thus be used for PID. It is not the particles themselves that are detected, but the electrons freed in the ionization. An electrode is located at the centre of the detector and a high voltage of -100 kV is applied to it. This voltage generates an electric field from the electrode to the endplates, parallel to the beam axis. This electric field will accelerate electrons to one of two anodes at the ends of the cylinder. The anode is a wire plane with wires in the azimuthal direction. The innermost wires are held at a potential of 1350 V and the outermost are held at a potential of 1550 V. When the electrons reach high enough energies, they will also start to ionize the gas, hereby producing secondary electrons. These secondary electrons will also start ionizing the gas, causing so called *avalanches*.

Each avalanche is collected by the nearest wire on the anode. The signal induced on the anode is transmitted to the pad plane directly behind the anode. This pad plane is divided into rows, which are circular bands in the azimuthal direction. These rows are in turn divided into pads. Each pad has the shape of a slightly bend square. Since the row is a circular band, the pads are all located at the same distance from the center of the endplate, but at different azimuthal angles. If the signal passes the treshold value in a pad, it will be labeled as a *cluster*. The maximum number of clusters of a track is 159, since this is the total number of rows in the TPC. From the position of the cluster on the pad plane the (x, y)-coordinates of the ionization event can be determined. From the drift time of the electron to the pad plane and the length of the track the z-coordinate of the ionization event can also be determined, and the track can thus be reconstructed.

The induced signal on the pad plane is proportional to the number of primary electrons. Knowing the number of primary electrons, the total energy loss of the particle can be determined and used for PID. Particles can be identified from energy loss measurements using the *Bethe-Bloch equation*, which is given by

$$\frac{\mathrm{d}E}{\mathrm{d}x} = \frac{4\pi}{m_e c^2} \cdot \frac{nz^2}{\beta^2} \cdot \left(\frac{e^2}{4\pi\epsilon_0}\right)^2 \cdot \left[\ln\left(\frac{2m_e c^2 \beta^2}{I \cdot (1-\beta^2)}\right) - \beta^2\right], \tag{2.1}$$

where $\frac{\mathrm{d}E}{\mathrm{d}x}$ is the energy loss of the particle, m_e is the rest mass of the electron, c is the speed of light, n is the electron number density of the target, z is the charge of the particle, β equals v/c, v is the velocity of the particle, e is the electron charge, ϵ_0 is the vacuum permittivity and I is the mean excitation potential of the target. A fit is performed to the $\mathrm{d}E/\mathrm{d}x$ distribution. The distribution around

that fit has a width σ_{TPC}. This width can be used to quantify how close the $\mathrm{d}E/\mathrm{d}x$ of a track is to the ideal $\mathrm{d}E/\mathrm{d}x$ of a certain particle species and can thus be used to identify the particles.

In addition, a magnetic field is also applied along the length of the cylinder. From the bending of the charged particles in this magnetic field the charge and the momentum of the particle can be determined. Furthermore, the TPC can also be used for centrality determination and the determination of the primary vertex.

2.2.3 Time of Flight (TOF)

The Time Of Flight is a cylindrical detector that is coaxial with the beam axis and surrounds the TPC. The TOF covers the pseudo-rapidity range $|\eta| < 0.9$ and has full azimuthal coverage. The TOF has an inner radius of 3.7 m, an outer radius of 3.99 m and a length of 7.41 m. The TOF measures the arrival time of the particle. Together with the time at which the collision took place, this can be used to determine the *time-of-flight*, which is the time it took for a particle to cross the detector. The combination of the time-of-flight from the TOF and the momentum measurements from the TPC can be used for particle identification of anti-protons, kaons and pions.

Using $p = \gamma m v$, the square of the mass of the particle can be written as

$$m^2 = \frac{p^2}{\gamma^2 v^2}, \tag{2.2}$$

where p is the momentum of the particle, γ the Lorentz factor and v the velocity of the particle. Using $\gamma = 1/\sqrt{1 - v^2/c^2}$, $v = t/L$, natural units ($c = 1$) and some rearranging, this can be written as

$$m^2 = p^2 \left(\frac{t^2}{L^2} - 1 \right), \tag{2.3}$$

where t is the time-of-flight and L the length of the track. So using the momentum measurements from the TPC, the time-of-flight measurements from the TOF and the length of the track the mass of the particle can be determined, and the particle can thus be identified. Just as in the case of PID using energy loss, the particles are distributed around the ideal value for a certain particle species with a width σ_{TOF}. PID using the TOF has a π/K separation better than $3\,\sigma_{TOF}$ for $p < 2.5$ GeV/c, and a K/p separation better than $3\,\sigma_{TOF}$ for $p < 4$ GeV/c.

2.2.4 VZERO

The VZERO detector consists of two arrays of scintillation counters, called VZERO-A and VZERO-C, placed on either side of the primary vertex. The VZERO-A detector is placed at $z = 3.4$ m and it covers the pseudo-rapidity range $2.8 < \eta < 5.1$. The VZERO-C is located at $z = -0.9$ m and it covers the pseudo-rapidity range $-3.7 < \eta < -1.7$. The VZERO serves as a trigger system and it can be used to determine the centrality of a collision, since it records the multiplicity of an event.

Chapter 3

Results

For this thesis the full data sample from run 1 of the LHC Pb-Pb runs in 2010 is used, which contains about 16 million minimum bias events (collisions). The analysis was performed within ROOT, which is a C++ based framework for data analysis developed by CERN.

3.1 Event and track selection

In order to remove tracks that are not suitable for the analysis, several cuts were placed on the events and tracks. Only events with a centrality lower than 80% are used. The VZERO detector is used to estimate the centrality of an event. As mentioned in Chapter 2, the TPC can also be used to estimate the centrality. A cut is placed on the absolute difference between the centrality estimated using the TPC (C_{VZERO}) and the centrality estimated using the TPC (C_{TPC}). If this difference is larger than 7.5%, the centrality of the track cannot be determined with enough accuracy and the event is rejected.

For the reconstructed vertex an event cut is also applied. The reconstructed vertex is measured along the z-axis (beam axis). If the distance from the reconstructed vertex to the center of the coordinate system, where the beams were designed to collide, is larger than 10 cm the event is rejected.

In addition, a momentum cut is applied to each track. Tracks with transverse momentum below 0.2 GeV/c or above 20 GeV/c are not accepted. The strong magnetic field will cause low momentum particles to spiral, instead of being bent lightly. This makes it difficult to measure low momentum particles. Tracks with high momentum are not used, since there are not enough tracks with high momentum to get good statistics.

Tracks are also cut on their pseudo-rapidity value. Only tracks with an absolute value of the pseudo-rapidity smaller than 0.8 are accepted.

The maximum number of clusters of a track is 159. Tracks with a number of clusters below 70 are rejected. When the number of clusters is too low, track reconstruction becomes harder and thus more inaccurate.

Tracks are also selected based on their energy loss $\mathrm{d}E/\mathrm{d}x$. Particles with an energy loss smaller than 10 are rejected.

A cut is also applied on the DCA, both in the xy-plane and in the z-direction. Tracks with a DCA_{xy} or a DCA_z larger than 3.2 cm are rejected. This cut is used to reduce the number of secondary particles, which do not come from the primary vertex, as discussed in Chapter 2. Since secondary particles do not come from the primary vertex, their DCA is larger than for primary particles. Table 3.1 summarizes the cuts placed on the events and the tracks.

3.2 Elliptic flow

The method used for calculating the elliptic flow is the scalar product method, as discussed in Chapter 1. In order to check that the method is working correctly, v_2 of unidentified particles is compared with ALICE preliminary results. The data was divided in nine different centrality classes: 0-5%, 5-10%, 10-20%, 20-30%, 30-40%, 40-50%, 50-60%, 60-70% and 70-80%. Figure 3.1 shows a histogram of the calculated v_2 as a function of transverse momentum for the different centrality classes.

Table 3.1: *Cuts used for event and track selection.*

Parameter	**Cut**
Centrality	$0\% < \mathrm{C} < 80\%$
Centrality difference	$\lvert C_{VZERO} - C_{TPC} \rvert < 7.5\%$
Reconstructed z-vertex	$V_z < 10$ cm
Transverse momentum	$0.2 < p_T < 20$ GeV/c
Pseudo-rapidity	$\lvert \eta \rvert < 0.8$
Number of clusters	$N_{cl} < 70$
Energy loss	$\mathrm{d}E/\mathrm{d}x > 10$
Distance of Closest Approach	$DCA_{xy} < 3.2$ cm $DCA_z < 3.2$ cm

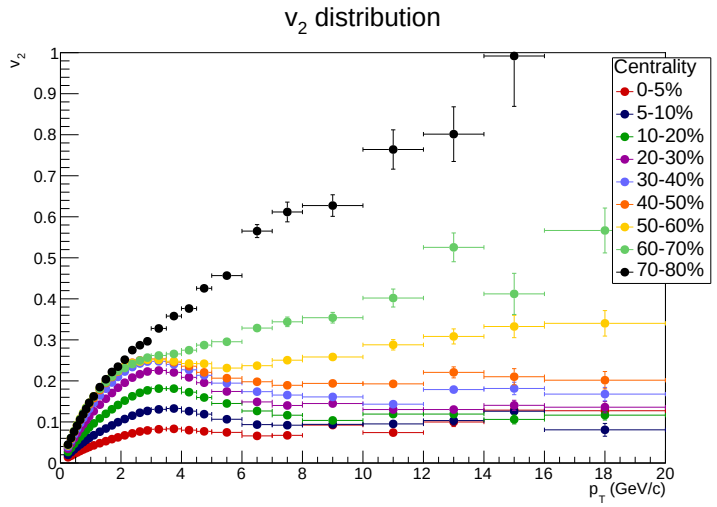

Figure 3.1: v_2 as a function of transverse momentum for all tracks for nine different centrality classes.

It can be seen that the unidentified v_2 increases with increasing p_T up until $p_T \approx 3$ GeV/c, after which is starts to decrease in the six lowest centrality classes (from 0% up until 50%). In the three highest centrality classes v_2 increases with p_T in the whole p_T range.

Figure 3.1 also shows that v_2 increases for increasing centrality. As discussed in Chapter 1, non-flow effects such as jets and resonances are also present in the scalar product method. These effects are primarily due to few particle correlations, and will thus be most present for low multiplicities. A higher centrality corresponds with a more peripheral collision and thus a lower multiplicity. Non-flow effects are therefore more present for higher centralities and increase v_2 in these centrality classes.

For the ALICE preliminary results a different binning was used, so in order to compare the two analyses a fit was done to the v_2 from this analysis using polynomials. Then both the ratio of the v_2 from this analysis to the fit and the ratio of the v_2 from the ALICE preliminary results to that same fit were computed. Since the ALICE preliminary results contain only data up until the centrality class 40-50%, the fitting and the comparison was done only in the first six centrality classes. Figure 3.2 and Figure 3.3 show the comparison of the analyses and the ratio's to the fit respectively.

In Figure 3.3 it can be seen that for $p_T > 1$ GeV/c the ratio of the v_2 from this analysis is within 1% agreement with the ratio of the v_2 from the ALICE preliminary results, for all centrality classes. For $p_T < 1$ GeV/c, the ratio of v_2 from the ALICE preliminary results to the fit is increasing with decreasing p_T for all centrality classes. This deviation is caused by secondaries. For the ALICE preliminary results a larger cut on the DCA was used, so those results contain more secondaries than the analysis from this thesis, and secondaries are most present at low p_T. For large p_T the statistical errors are large, due to the fact that there are less high momentum tracks. This makes the calculation of v_2 inaccurate, but within the error bars the analysis is in agreement with the ALICE preliminary results. The fact that the analysis is within 1% agreement with the ALICE preliminary results for $p_T > 1$ GeV/c shows that the

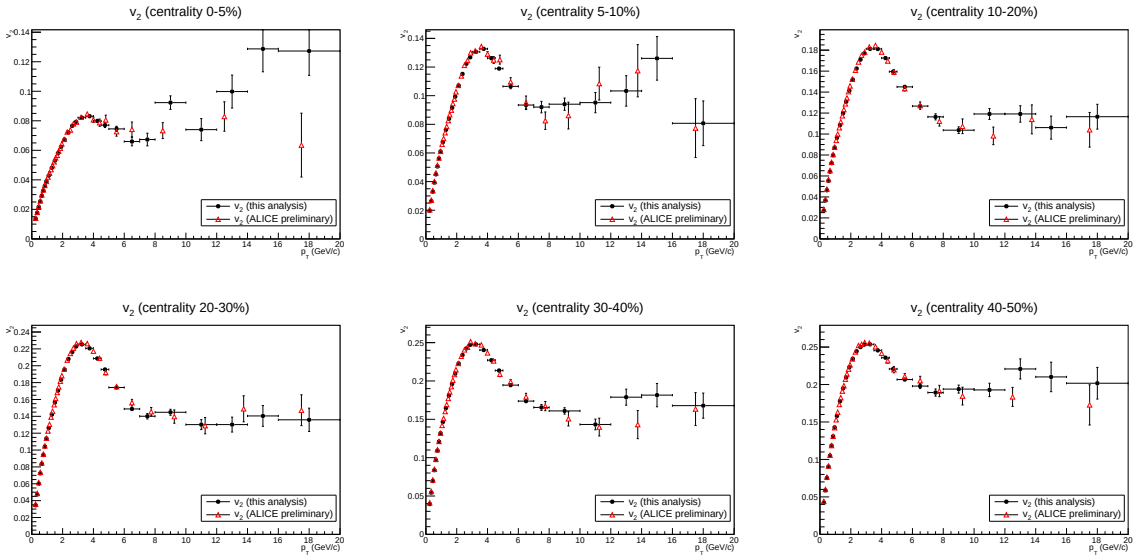

Figure 3.2: v_2 calculated in this thesis before PID (black) compared to the v_2 of the ALICE preliminary results (red) for six different centrality classes, in the range $0 < p_T < 20$ GeV/c.

method used for calculating v_2 is effective.

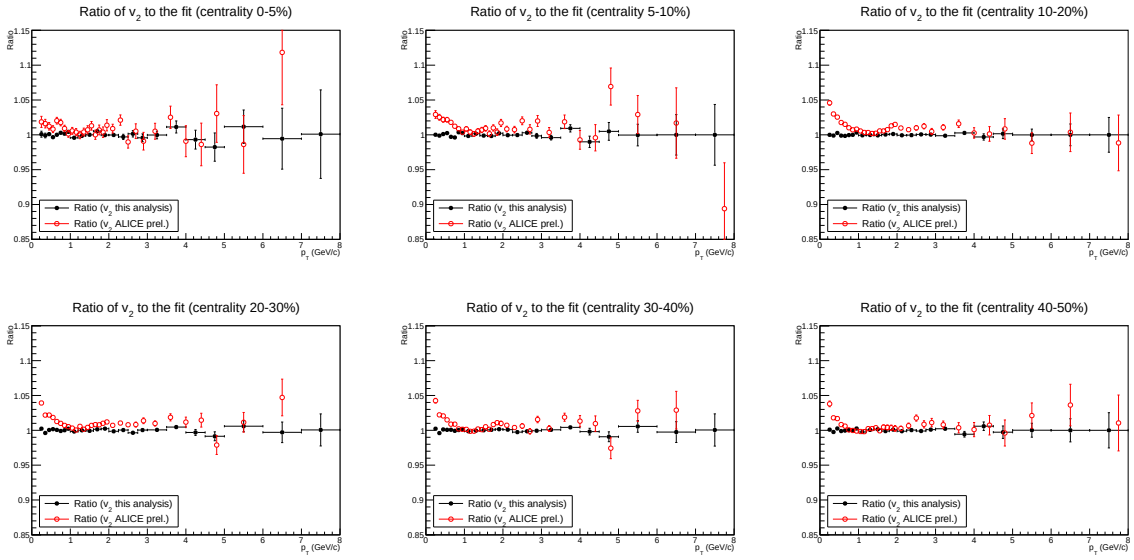

Figure 3.3: The ratio's of both the v_2 that was calculated in this thesis to the fit (black) and the ratio of v_2 from the ALICE preliminary results to that same fit (red), in the range $0 < p_T < 8$ GeV/c. The fact that the ratio of the ALICE preliminary results to the fit that was done to this analysis is within 1% for $p_T > 1$ GeV/c shows that this analysis is in good agreement with the ALICE preliminary results.

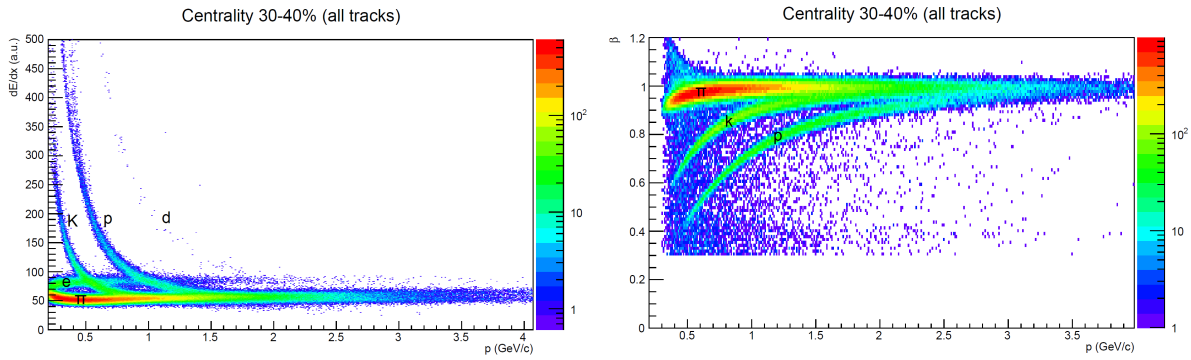

(a) (b)

Figure 3.4: For PID two methods are combined. (a) Energy loss measurements from the TPC can be compared with the theoretical prediction from the Bethe equation to determine the particle species. (b) Using the time-of-flight from the TOF and the momentum measurement of the TPC, the mass of the particle can be determined, hereby identifying the particle.

3.2.1 Particle identification

The identification of the particles was accomplished using both measurements from the TPC and the TOF. The TPC is used for energy loss measurements, which can then be used for particle identification using the Bethe-Bloch equation, as discussed in Chapter 2. In the case of the TOF the combined measurements of the time-of-flight in the TOF and the momentum in the TPC yield the particle mass and hereby identify it. Figures 3.4 shows that different particle species can clearly be distinguished using these methods.

As discussed in Chapter 2, the PID that was done using the TPC gives a distribution with a width $\sigma_{TPC,i}$ for particle species i and the PID that was done using the TOF gives a width $\sigma_{TOF,i}$. For particles with momentum $p_T < 0.4$ GeV/c only the measurements from the TPC are used for PID, since low momentum particles do not reach the TOF. For particles with momentum $p_T > 0.4$ GeV/c both information from the TOF and the TPC is combined, with the width calculated as $\sigma_i = \sqrt{\sigma^2_{TPC,i} + \sigma^2_{TOF,i}}$, with $i = \bar{p}, K, \pi$. For each track the σ_i's are compared, and the lowest one is determined. The particle species i that corresponds to this minimum width is then assigned to the track, with the condition that $\sigma_i < 3$, otherwise the track is rejected. Tracks for which σ_p, σ_K and σ_π are equal are also rejected, since then PID is not possible.

The method used for PID is reliable only for low momentum. For anti-protons and pions tracks with momentum $p_T < 4$ GeV/c can be used. Kaons show more contamination from other particle species and can therefore only be used for $p_T < 3$ GeV/c. The reason for this is that in Figures 3.4a and 3.4b the kaons are between the pions and the protons, so the contamination for kaons comes from both pions and protons.

Using these methods for PID the elliptic flow was calculated for anti-protons, kaons and pions separately. Figure 3.5 shows the results for different centrality classes. Anti-protons were used because anti-protons contain less secondaries than protons. The secondaries for protons come from material interactions and weak decays. By choosing for anti-protons the secondaries only originate from weak decays. For kaons and pions both the positive and negative particles were used. In Figure 3.6 the results for the different particle species are compared for each centrality class. It can clearly be seen that below 2 GeV/c the results show mass ordering. Mass ordering was predicted by the hydrodynamic model, as discussed in Section 1.3. The results are thus in qualitative agreement with the hydrodynamic model up until $p_T = 2$ GeV/c. However, at $p_T = 2$ GeV/c crossing of the particle species takes place and for $p_T > 2$ GeV/c mass ordering is no longer visible. The crossing of the particle species is an indication for particle production via quark coalescence, since this increases the baryon v_2 (anti-proton) relative to the meson v_2 (pion and kaon).

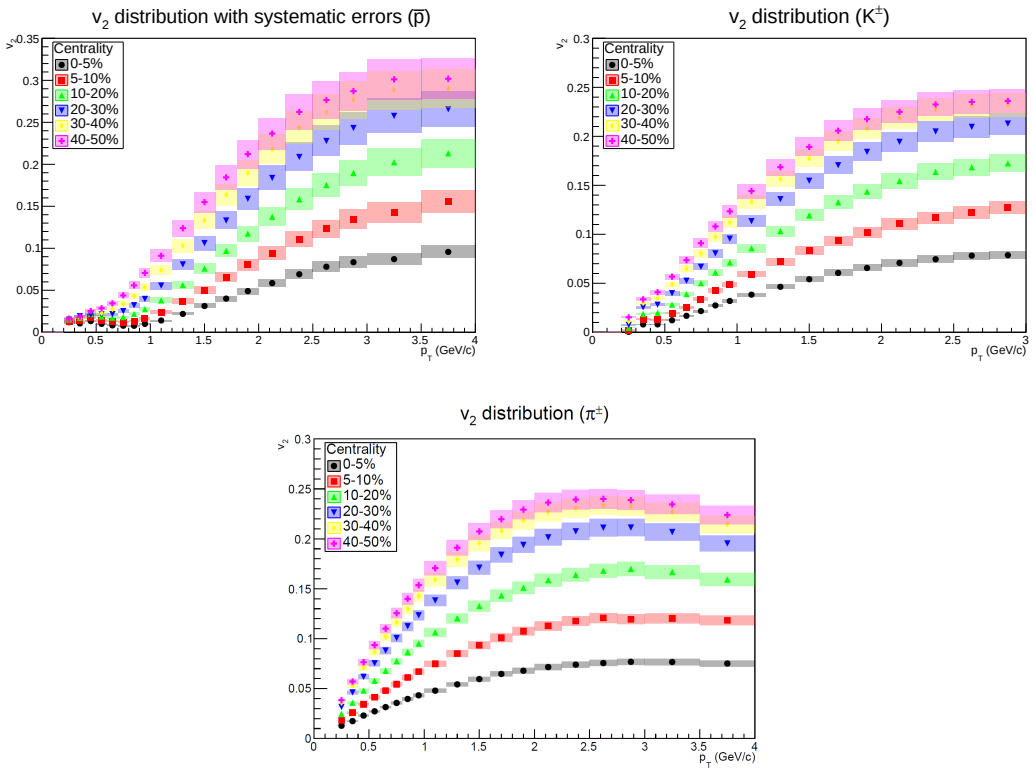

Figure 3.5: The elliptic flow coefficient v_2 calculated for anti-protons, kaons and pions separately for all six centrality classes.

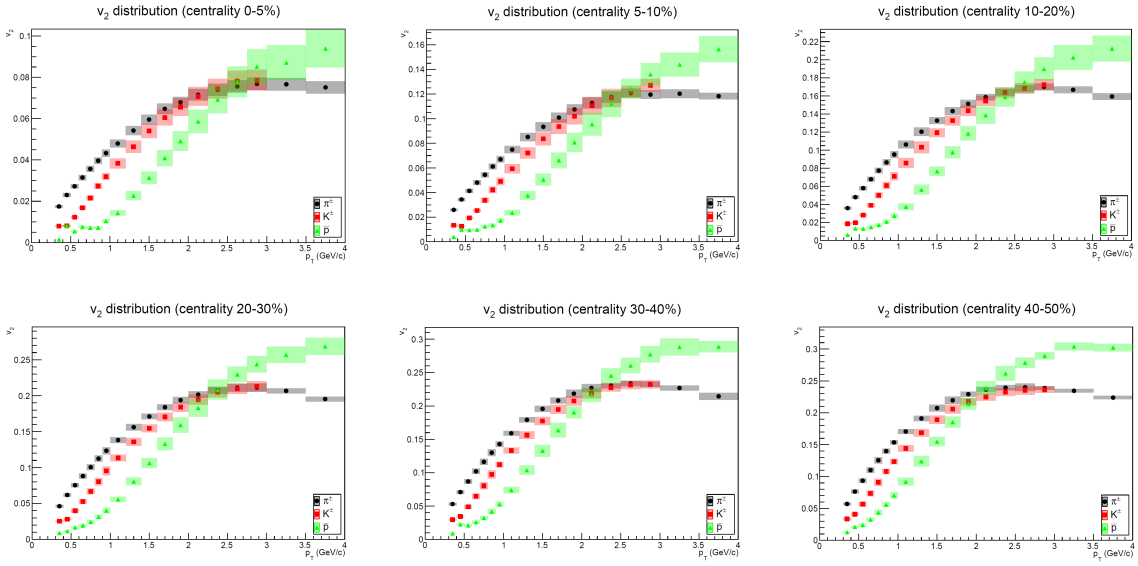

Figure 3.6: v_2 calculated for pions (black), kaons (red) and anti-protons (green) separately in three different centrality classes. For $p_T < 2$ GeV/c mass ordering, as predicted by hydrodynamic modelling, is clearly visible.

3.2.2 Systematic errors

The errors in Figure 3.6 are systematic errors, which were calculated for each particle species for all six centrality classes and in all 27 p_T bins separately. In order to calculate the systematic error due to each parameter v_2 was calculated again, but with a different cut for that parameter. For each parameter two or three different cuts were used, so v_2 was recalculated two or three times. Table 3.2 shows the extra cuts used to calculate the systematic errors.

Table 3.2: *Cuts used to calculate the systematic errors.*

Parameter	**Standard cut**	**Extra cuts**
Centrality detector	VZERO	TPC, SPD
Reconstructed z-vertex	$V_z < 10$ cm	$V_z < 5{,}7$ cm
Number of clusters	$N_{cl} < 70$	$N_{cl} < 80$, 90
Distance of Closest Approach	$DCA_{xy} < 3.2$ cm $DCA_z < 3.2$ cm	$DCA_{xy} < 0.5, 1, 2$ cm $DCA_z < 0.5, 1, 2$ cm
PID (σ)	$\sigma < 3$	$\sigma < 1, 2$
Charge	Mixed	Positive, negative
Magnetic field	Mixed	Positive, negative

Both for DCA_{xy} and DCA_z a correction had to be applied to the recalculated v_2. By decreasing the cut on the DCA, tracks are removed from the data. This can result in dips in the $\phi-$distribution. The method requires that the $\phi-$distribution be flat, and therefore the non-uniformity acceptance (NUA) has to be corrected. Before calculating the systematic errors, the NUA correction was applied in the calculation of the v_2 for all extra cuts and also for the standard cut. The NUA corrected v_n is calculated as

$$v_n\{NUA\} = \frac{\left\langle\left\langle u_{n,i}(p_T, y)\frac{Q_n^*}{M}\right\rangle\right\rangle - \langle\langle\cos[n\phi]\rangle\rangle_{RP}\cdot\langle\langle\cos[n\phi]\rangle\rangle_{POI} - \langle\langle\sin[n\phi]\rangle\rangle_{RP}\cdot\langle\langle\sin[n\phi)]\rangle\rangle_{POI}}{\sqrt{\left\langle\frac{Q_n^a}{M_a}\frac{Q_n^{b*}}{M_b}\right\rangle - \left\langle\frac{Q_a^x}{M_a}\right\rangle\left\langle\frac{Q_b^x}{M_b}\right\rangle - \left\langle\frac{Q_a^y}{M_a}\right\rangle\left\langle\frac{Q_b^y}{M_b}\right\rangle}}. \tag{3.1}$$

For each extra cut for a parameter the recalculated v_2 was divided by the standard v_2. The recalculated v_2 and the standard v_2 contain the same tracks and are thus fully correlated. Therefore, the statistical errors of the ratio's were overestimated and recalculated as $\sigma = \sqrt{|\sigma_c^2 - \sigma_s^2|}$, where σ_c is the old statistical error for the changed v_2 and σ_s is the old statistical error for the standard v_2.

Only for the magnetic field and the charge the calculation of the ratio's was done differently. In these cases the tracks were divided into two groups based on positive and negative magnetic fields and positive and negative charges respectively. The elliptic flow was recalculated with only the positive or the negative magnetic fields or charges. Then the ratio of the v_2 obtained from only the positive magnetic fields or positive charges to v_2 obtained from only the negative magnetic fields or negative charges was calculated. Since in this case the recalculated and default v_2 do not contain the same tracks, they are not correlated. The statistical errors are therefore not overestimated and they need not be recalculated.

Figure 3.7 shows the obtained ratio's for the three particle species in all six centrality classes. The ratio's tend to fluctuate around a constant. To remove these fluctuations the ratio was fit with a constant. For some parameters the ratio decreased or increased for $p_T < 1$ GeV/c, so the ratio no longer fluctuates around that constant. In these cases only the part of the ratio that fluctuates around a constant was fit, which was always for $p_T > 1$ GeV/c. For $p_T < 1$ GeV/c the ratio was used directly instead of the fit.

The systematic errors due to a parameter are calculated as $\sigma_{par}(p_T) = |RF(p_T) - 1| \times 100\%$, with $RF(p_T)$ either the value of the ratio or the fit in the corresponding p_T bin. Since for each parameter two or three extra cuts were used, two or three ratio's and thus two or three systematic errors were obtained. For each parameter the maximum of these systematic errors is assigned as the systematic error due to that parameter. Then the total systematic error due to all parameters for a specific p_T bin is calculated as

$$\sigma_{syst}(p_T) = \sqrt{\sigma_{cent}^2 + \sigma_{charge}^2 + \sigma_{DCA_{xy}}^2 + \sigma_{DCA_z}^2 + \sigma_{mag}^2 + \sigma_{N_{cl}}^2 + \sigma_{PID}^2 + \sigma_{V_z}^2}. \tag{3.2}$$

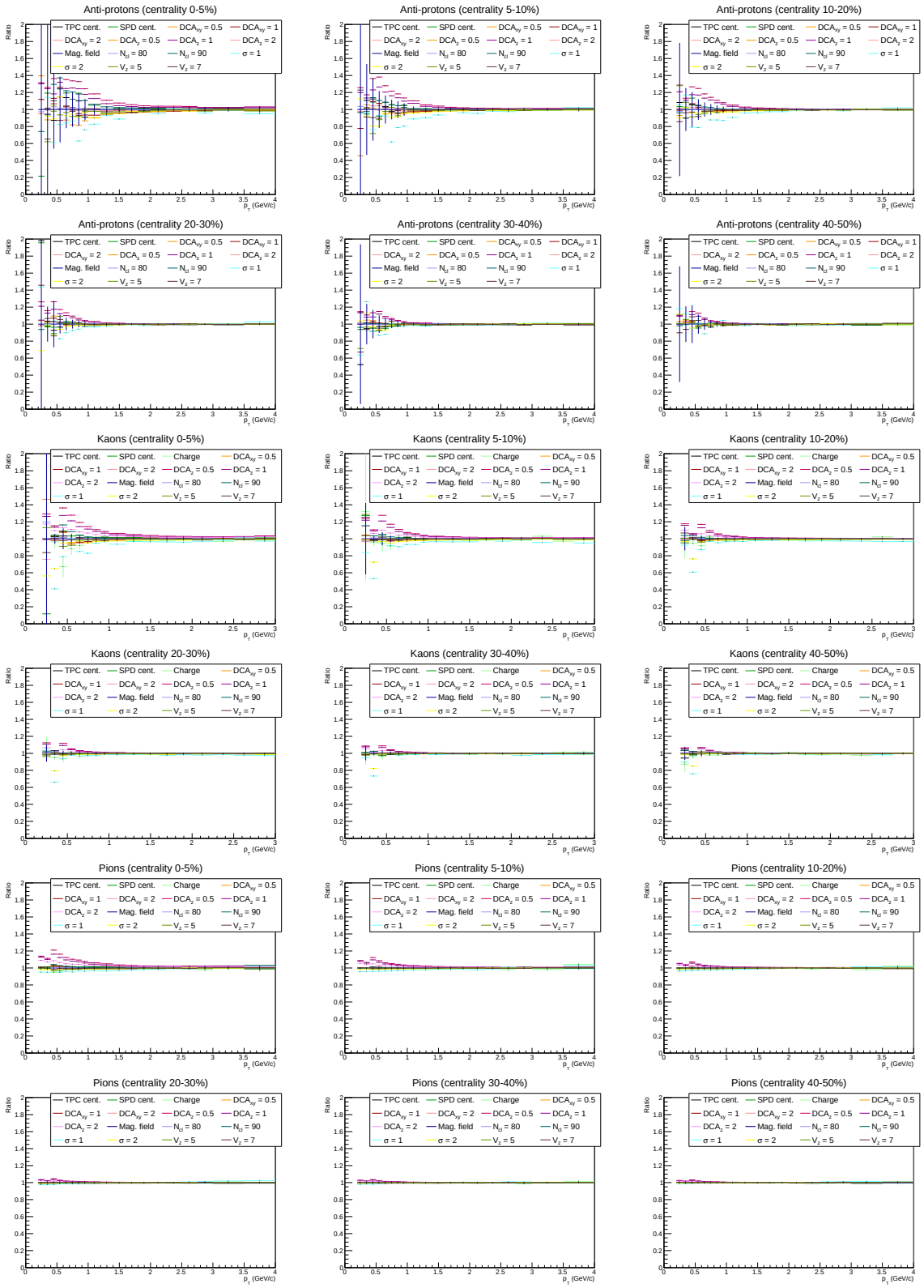

Figure 3.7: *The ratio's of v_2 obtained with an extra cut to the v_2 contained with the default cut plotted for all parameters for each particle species and in each centrality class.*

For $p_T \geq 1$ GeV/c the systematic errors in all p_T bins are equal since in this p_T range the fit is always

used to determine the systematic error. For $p_T < 1$ GeV/c the systematic errors can differ per p_T bin, since for some parameters in this p_T range the ratio was used directly. Table 3.3 shows the systematic errors for the bin $0.3 < p_T < 0.4$. Table 3.4 shows the systematic errors for $p_T \geq 1$ GeV/c. The systematic errors seem to decrease with increasing centrality. This same effect can be seen in Figure 3.6. The systematic error due to the PID (σ) is highest. Changing this parameter will influence the purity of the samples of anti-protons, kaons and pions. When the cut on σ is lower, the purity is increased and this will of course alter the v_2. It can also be seen in Figure 3.7 that the ratio's for the recalculated v_2 with a different σ cut decrease for $p_T < 1$ GeV/c. This is due to the removal of secondaries, which are most present at low p_T.

For the magnetic field on the other hand, the systematic error is zero for all p_T bins, centrality classes and particle species. This also makes sense, since the sign of the magnetic field should have no effect on the experiment. The particle tracks will merely be bend in opposite direction, but this should not influence v_2.

The total systematic error in Table 3.4 is largest for anti-protons and smallest for pions. This might be because more pions are produced in the collisions than kaons and anti-protons. This is because pions are the lightest particles of the three and are thus easiest to produce, and anti-protons are the heaviest and thus hardest to produce. Therefore the data contains most pions and least anti-protons. This should not influence the systematic errors, but it is possible that somehow the statistical errors got into the systematic errors.

For anti-protons a systematic charge error could not be assigned, since protons were not used in the analysis.

Table 3.3: *The systematic errors for the p_T bin $0.3 < p_T < 0.4$ due to all eight parameters, for anti-protons, kaons and pions separately.*

Parameter	**Cent. 0-5%**	**5-10%**	**10-20%**	**20-30%**	**30-40%**	**40-50%**
Centrality	1.4	0.3	0.7	0.8	0.7	0.5
Charge	1.3	0.5	0.3	0.2	0.2	0.2
DCA_{xy}	1.0	1.0	1.0	1.0	1.0	1.0
DCA_z	1.0	1.0	1.0	1.0	1.0	1.0
Magnetic field	0	0	0	0	0	0
Number of clusters	1.0	1.0	1.0	1.0	1.0	1.0
PID (σ)	2.9	1.9	1.3	0.6	0.2	0.0
z-vertex	4.1	1.0	1.0	1.0	1.0	1.0
Total error	**4.0**	**2.9**	**2.7**	**2.4**	**2.4**	**2.3**

(a) Pions

Parameter	**Cent. 0-5%**	**5-10%**	**10-20%**	**20-30%**	**30-40%**	**40-50%**
Centrality	1.0	1.0	1.0	1.0	1.0	1.0
Charge	1.7	0.1	0.6	0.5	0.3	0.1
DCA_{xy}	1.0	1.0	1.0	1.0	1.0	1.0
DCA_z	1.0	1.0	1.0	1.0	1.0	1.0
Magnetic field	0	0	0	0	0	0
Number of clusters	1.0	1.0	1.0	1.0	1.0	1.0
PID (σ)	4.2	3.2	2.3	1.6	1.1	0.9
z-vertex	0.6	1.0	1.1	1.0	1.0	1.1
Total error	**5.1**	**4.0**	**3.4**	**3.0**	**2.7**	**2.6**

(b) Kaons

Parameter	**Cent. 0-5%**	**5-10%**	**10-20%**	**20-30%**	**30-40%**	**40-50%**
Centrality	1.0	0.9	0.9	1.0	0.9	1.0
DCA_{xy}	0.9	1.1	1.0	1.0	1.0	1.0
DCA_z	1.1	1.0	1.0	1.1	1.0	1.0
Magnetic field	0	0	0	0	0	0
Number of clusters	0.9	1.0	1.0	1.0	1.0	1.0
PID (σ)	7.6	6.3	4.1	1.6	1.0	0.7
z-vertex	0.6	1.0	1.1	1.0	1.0	1.1
Total error	**8.0**	**6.8**	**4.8**	**2.9**	**2.6**	**2.5**

(c) Anti-protons

Table 3.4: *The systematic errors for $p_T \geq 1$ GeV/c due to all eight parameters, for anti-protons, kaons and pions separately.*

Parameter	**Cent. 0-5%**	**5-10%**	**10-20%**	**20-30%**	**30-40%**	**40-50%**
Centrality	1.4	0.3	0.7	0.8	0.7	0.5
Charge	1.3	0.5	0.3	0.2	0.2	0.2
DCA_{xy}	0.7	0.3	0.1	0.1	0.1	0.1
DCA_z	1.3	0.6	0.3	0.2	0.1	0.1
Magnetic field	0	0	0	0	0	0
Number of clusters	0.2	0.4	0.4	0.4	0.3	0.3
PID	2.9	1.9	1.3	0.6	0.2	0.0
z-vertex	0.7	0.4	0.2	0.05	0.0	0.1
Total error	**4.0**	**2.3**	**1.7**	**1.2**	**0.9**	**0.7**

(a) Pions

Parameter	**Cent. 0-5%**	**5-10%**	**10-20%**	**20-30%**	**30-40%**	**40-50%**
Centrality	1.2	0.3	0.7	0.8	0.6	0.4
Charge	1.7	0.1	0.6	0.5	0.3	0.1
DCA_{xy}	4.0	0.6	0.3	0.2	0.1	0.0
DCA_z	1.5	0.6	0.3	0.2	0.1	0.1
Magnetic field	0	0	0	0	0	0
Number of clusters	0.0	0.4	0.4	0.4	0.3	0.3
PID (σ)	4.2	3.2	2.3	1.6	1.1	0.9
z-vertex	0.4	0.8	0.4	0.2	0.3	0.3
Total error	**6.4**	**3.5**	**2.6**	**2.0**	**1.5**	**1.1**

(b) Kaons

Parameter	**Cent. 0-5%**	**5-10%**	**10-20%**	**20-30%**	**30-40%**	**40-50%**
Centrality	1.9	0.4	1.0	0.9	0.9	0.8
DCA_{xy}	4.2	1.6	0.7	0.4	0.4	0.4
DCA_z	2.2	1.1	0.6	0.2	0.1	0.1
Magnetic field	0	0	0	0	0	0
Number of clusters	2.2	0.3	0.2	0.3	0.3	0.2
PID (σ)	7.6	6.3	4.1	1.6	1.0	0.7
z-vertex	2.4	0.8	0.4	0.2	0.3	0.3
Total error	**9.7**	**6.7**	**4.4**	**2.0**	**1.6**	**1.2**

(c) Anti-protons

Chapter 4

Conclusions and outlook

The elliptic flow analysis is within 1% agreement with the ALICE preliminary results for $p_T > 1$ GeV/c. It is only for small p_T that the analysis shows deviations from the ALICE preliminary results, which are caused by secondaries. For high p_T the errors bars are large due to the small number of high momentum tracks, but within the error bars the results are in good agreement with the ALICE preliminary results.

The results show a correlation between the elliptic flow v_2 and the centrality. The elliptic flow increases for increasing centrality. This effect is explained by non-flow effects, which increase for decreasing multiplicity, as discussed in Chapter 1. The non-flow effects are mostly present for few particle correlations. The analysis could thus be improved by taking into account higher order particle correlations. In this thesis the particle identified elliptic flow was calculated up until the centrality class 40-50%. It would be interesting to also calculate the elliptic flow for higher centralities, especially when more of the non-flow effects are removed.

PID was done using energy loss measurements from the TPC and time-of-flight measurements from the TOF. This method can only be used up to $p_T = 4$ GeV/c for anti-protons and pions and up until $p_T = 3$ GeV/c for kaons. It would be interesting to see what happens for higher momentum. This could be accomplished with other methods for PID, which allow you to explore a larger momentum range. In the current analysis the statistics for high momentum particles are bad, due to the low number of tracks. So next to a different PID method, more data would also have to be available in order to go to higher p_T ranges.

The systematic errors increase with decreasing centrality. The systematic errors are highest for anti-protons, intermediate for kaons and lowest for pions. This effect could not be explained. It might be possible that the statistical errors somehow got into the systematic errors.

The data shows mass ordering up until $p_T = 2$ GeV/c. This is in qualitative agreement with the hydrodynamic model. For this thesis it was not possible to compare the elliptic flow quantitatively with the hydrodynamic model, since only a qualitative comparison model was available (Figure 1.5). It would also be interesting to compare the analysis quantitatively with the hydrodynamic model and from this extract the initial conditions, η/s and the equation of state. Maybe the analysis could also be performed for additional particle species, to see if they are also in agreement with the hydrodynamic model.

For $p_T > 2$ GeV/c the elliptic flow shows crossing of the particle species, which is in indication of quark coalescence. If the analysis would be performed for a larger p_T range it would be interesting to see if it is possible to compare the results with predictions for quark coalescence in that p_T range.

Appendix A

The ALICE coordinate system

The global ALICE coordinate system is a right-handed, orthogonal Cartesian coordinate system. Its origin is located at the interaction point of the beams. The x-axis is defined to be perpendicular to the mean beam direction, with the positive x-direction pointing towards the centre of the LHC ring. The y-axis is perpendicular to both the beam direction and the x-axis, with its positive direction pointing upward. The z-axis is parallel to the beam direction, with its positive direction in the counterclockwise direction. The azimuthal angle ϕ is in the xy-plane. It increases from the positive x-axis ($\phi = 0$) to the positive y-axis ($\phi = \pi/2$), with its total range being between 0 and 2π. The polar angle θ is in the yz-plane and it increases from the positive z-axis ($\theta = 0$) to the positive y-axis ($\theta = \pi/2$), with its total range being between 0 and π [20]. Figure A.1 shows the ALICE detector with the global ALICE coordinate system.

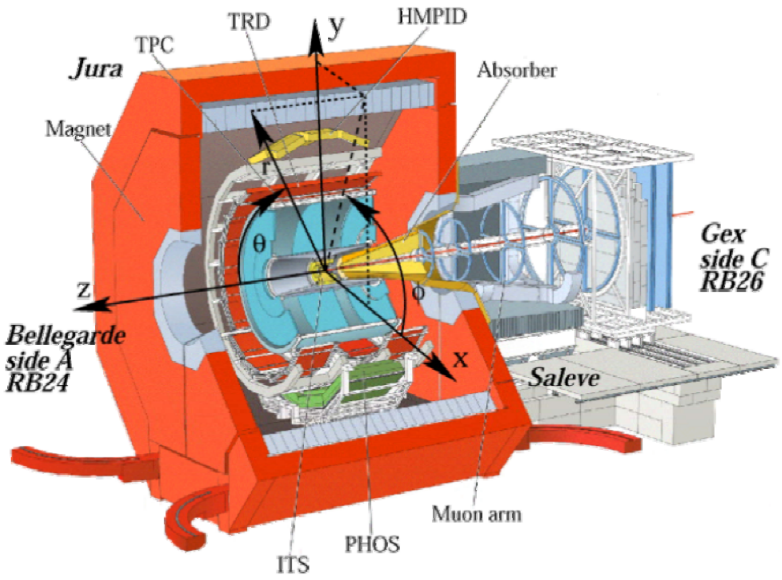

Figure A.1: The global ALICE coordinate system. Figure taken from [20].

Acknowledgements

I would like to thank my supervisor prof. dr. R.J.M. Snellings for giving me the opportunity to do this research and for his guidance and supervision throughout the project.

Many thanks go to my daily supervisor dr. A.F. Dobrin for all his help. Thanks for always taking the time to answer my questions, for explaining the import concepts over and over and for helping me solve my coding problems.

References

[1] K. G. Wilson. Confinement of Quarks. *Phys.Rev.*, D10:2445–2459, 1974. doi: 10.1103/PhysRevD.10.2445.

[2] Zajc W.A. Riordan, M. The first few micro-seconds. *Sci.Am.*, 24:294, 2006.

[3] Cameron P. Cerniglia P. *et al.* Bai, M. Rhic beam instrumentation. *Nucl. Instrum. Meth.*, A 499.

[4] K. Aamodt and others. (ALICE Collaboration). The alice experiment at the cern lhc. *Journal of Instrumentation*, 3(08):S08002, 2008. URL `http://stacks.iop.org/1748-0221/3/i=08/a=S08002`.

[5] R.A. Bertens. Azimuthal anisotropy of θ-mesons in $\sqrt{S_{NN}} = 2.76$ tev pb-pb collisions at alice. Master's thesis, Utrecht University, 2012.

[6] Bjorn Schenke, Sangyong Jeon, and Charles Gale. Elliptic and triangular flow in event-by-event (3+1)D viscous hydrodynamics. *Phys.Rev.Lett.*, 106:042301, 2011. doi: 10.1103/PhysRevLett.106.042301.

[7] Larry D. McLerran and Raju Venugopalan. Computing quark and gluon distribution functions for very large nuclei. *Phys.Rev.*, D49:2233–2241, 1994. doi: 10.1103/PhysRevD.49.2233.

[8] R.J.M. Snellings. Elliptic Flow: A Brief Review. *New J.Phys.*, 13:055008, 2011. doi: 10.1088/1367-2630/13/5/055008.

[9] C. Shen. Relativistic heavy ion collisions, 11 May 2015. URL `https://u.osu.edu/vishnu/files/2014/09/little_bang-10wt2pd.jpg`.

[10] R.J.M. Snellings. Collective Expansion at the LHC: selected ALICE anisotropic flow measurements. *J.Phys.*, G41(12):124007, 2014. doi: 10.1088/0954-3899/41/12/124007.

[11] B. Müller. The 'Perfect' Fluid Quenches Jets Almost Perfectly. *Prog.Part.Nucl.Phys.*, 62:551, 2009. doi: 10.1016/j.ppnp.2008.12.028.

[12] S. Voloshin and Y. Zhang. Flow study in relativistic nuclear collisions by Fourier expansion of Azimuthal particle distributions. *Z.Phys.*, C70:665–672, 1996. doi: 10.1007/s002880050141.

[13] Sergei A. Voloshin, Arthur M. Poskanzer, and Raimond Snellings. Collective phenomena in non-central nuclear collisions. 2008.

[14] P. Huovinen, P.F. Kolb, Ulrich W. Heinz, Ruuskanen P.V., and S.A. Voloshin. Radial and elliptic flow at RHIC: Further predictions. *Phys.Lett.*, B503:58–64, 2001. doi: 10.1016/S0370-2693(01)00219-2.

[15] R.J.M. Snellings. Resonance Workshop at Catania. November 2014.

[16] R.J.M. Snellings, Arthur M. Poskanzer, and S.A. Voloshin. Anisotropic flow at STAR. 1999.

[17] CERN. The accelerator complex, 23 March 2015. URL `http://home.web.cern.ch/about/accelerators`.

[18] CERN, 23 March 2015. URL `http://te-dep-epc.web.cern.ch/te-dep-epc/machines/pagesources/Cern-Accelerator-Complex.jpg`.

[19] CERN, 17 May 2015. URL http://alipub-dev.web.cern.ch/.

[20] L. Betev and P. Chochula. Definition of the alice coordinate system and basic rules for subdetector components numbering, 2003. URL https://alice-servotech.web.cern.ch/ALICE-ServoTech/HELP_DCDB-SVT/Help_Files/ALICE-INT-2003-038.pdf.